ACS APPLIED MATERIALS & INTERFACES

www.acsami.org

Research Article

Surface Restructuring of Thin-Film Electrodes Based on Thermal History and Its Significance for the Catalytic Activity and Stability at the Gas/Solid and Solid/Solid Interfaces

Ozden Celikbilek,* Andrea Cavallaro, Gwilherm Kerherve, Sarah Fearn, Odette Chaix-Pluchery, Ainara Aguadero, John A. Kilner, and Stephen J. Skinner

Cite This: *ACS Appl. Mater. Interfaces* 2020, 12, 34388–34401

Read Online

ACCESS | Metrics & More | Article Recommendations | Supporting Information

ABSTRACT: Electrodes in solid-state energy devices are subjected to a variety of thermal treatments, from film processing to device operation at high temperatures. All these treatments influence the chemical activity and stability of the films, as the thermally induced chemical restructuring shapes the microstructure and the morphology. Here, we investigate the correlation between the oxygen reduction reaction (ORR) activity and thermal history in complex transition metal oxides, in particular, $La_{0.6}Sr_{0.4}CoO_{3-\delta}$ (LSC64) thin films deposited by pulsed laser deposition. To this end, three ∼200 nm thick LSC64 films with different processing and thermal histories were studied. A variety of surface-sensitive elemental characterization techniques (*i.e.*, low-energy ion scattering, X-ray photoelectron spectroscopy, and secondary ion mass spectrometry) were employed to thoroughly investigate the cationic distribution from the outermost surface to the film/substrate interface. Moreover, electrochemical impedance spectroscopy was used to study the activity and the stability of the films. Our investigations revealed that, despite the initial comparable ORR activity at 600 °C, the degradation rates of the films differed by twofold in the long-term stability tests at 500 °C. Here, we emphasize the importance of processing and thermal history in the elemental surface distribution, especially for the stability of LSC64 electrodes and propose that they should be considered as among the main pillars in the design of active surfaces.

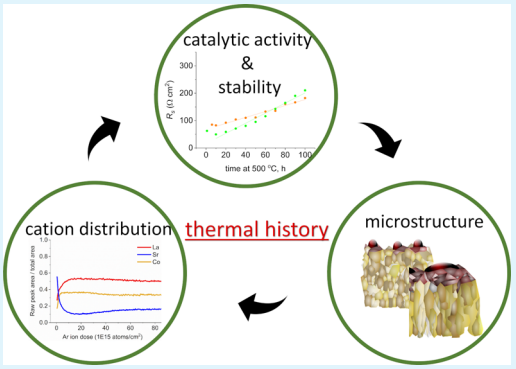

KEYWORDS: *solid oxide cells, thin films, thermal history, surface restructuring, cation redistribution, microstructure, segregation*

1. INTRODUCTION

The demand for stable and high-power density power sources has increased substantially over the last decade. As a result, the search for new ion- and electron-conducting metal-oxide materials, as well as innovative concepts and designs for energy conversion and storage devices has accelerated.[1] Notably, considerable attention was given to thin-film deposition techniques, such as pulsed laser deposition (PLD), as many exciting properties including conductivity and ion exchange/diffusion kinetics have been shown to be tuned by the defect structure. Defect features such as lattice strain, structural defects, space charge at the interface and local chemical composition are all proposed to affect mass transport significantly.[2]

At this point, it is important to highlight the importance of the thermal history of the films, which comprises any heat treatment from coating temperature to post thermal annealing. Besides, the requirement for operational temperatures exceeding 500 °C in ceramic solid oxide cells (SOC) leads to highly dynamic solid/solid and solid/gas interfaces because of both compositional and microstructural changes.[3] Therefore, thermally induced transformations occurring at the nanometer scale and below must be taken into account as they can be detrimental to the catalytic activity, including the segregation of inactive phases toward the surfaces,[4] particle formation and coarsening,[5] phase transitions, and decomposition at high temperatures.[6] The preparation technique,[7] coating conditions [substrate temperature ($T_{substrate}$), background oxygen pressure (pO_2) *etc.*],[8] crystallization behavior,[9] and thermal history[10] of the samples have been shown to influence the electrochemical activity but often remain unreported in the literature.

In terms of material choice, it is known that the amount of Sr dopant in $La_{1-x}Sr_xCoO_{3-\delta}$ (LSC) strongly alters the electronic band structure,[11] oxygen nonstoichiometry and transport properties,[12] concentration of segregated strontium

Received: May 6, 2020
Accepted: July 6, 2020
Published: July 6, 2020

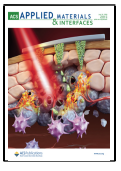

particles,[13] and oxygen reduction reaction (ORR) kinetics.[14,15] Among the LSC-based thin-film family ($0 \leq x \leq 0.8$), the optimal Sr content in terms of the highest electronic conductivity and fast ORR kinetics was found at $x = 0.4$.[15] Earlier works on $La_{0.6}Sr_{0.4}CoO_{3-\delta}$ (LSC64) thin films explored the relationship between the ORR activity and stability as a function of $T_{substrate}$.[16−19] Among the pioneers, Januschewsky *et al.* studied the electrode resistance values and degradation behavior of the LSC64 PLD films grown at various $T_{substrate}$ (*e.g.*, 200−700 °C).[16] They reported an optimal $T_{substrate}$ regime between 340 and 510 °C and these films exhibited better stability at 600 °C operation temperature. Evans *et al.*'s findings also confirmed that films grown at $T_{substrate}$ = 450 °C provided relatively low area-specific resistance values (0.3 Ω cm^2 at 400 °C).[17] Cai *et al.* reported similar results, showing both the activity and stability of films grown at $T_{substrate}$ = 450 °C being superior to those of $T_{substrate}$ = 650 °C.[19]

Common ground in the works mentioned above[16−19] is that the films were reported to have columnar microstructures. Notably for the columnar microstructure, Kubicek *et al.* revealed ∼3 orders of magnitude faster Sr diffusion along the grain boundaries than within the grains of LSC64 thin films.[20] Later, Rupp *et al.* showed that the Sr-rich surface layer could be removed by ultrapure water.[21] However, a new Sr-rich layer formed again at temperatures ≥550 °C. The authors suggested that the formation of the Sr-rich layer at high temperatures is an equilibrium process in the LSC films. Recent works investigated the correlation between surface composition, film processing temperature, and postannealing and etching on perovskite $SrTi_{0.65}Co_{0.35}O_{3-\delta}$, $SrTi_{0.65}Fe_{0.35}O_{3-\delta}$ and Ruddlesden−Popper $Sr_2Ti_{0.65}Fe_{0.35}O_{4\pm\delta}$ thin films.[22,23] The authors observed higher values for the chemical surface exchange coefficient for films grown below and up to the crystallization temperature compared with the well-crystalline films grown at high temperatures. Moreover, Cavallaro *et al.*[24] studied the oxygen ion transport dynamics in $La_{0.8}Sr_{0.2}CoO_{3-\delta}$ (LSC82) thin-films grown by PLD between $T_{substrate}$ = 200−750 °C. The authors observed that low-temperature-grown films exhibited a faster oxygen self-diffusion coefficient (D^*) and surface-exchange coefficient (k^*) compared with films grown at high temperatures. Electrochemical characterizations of these films showed an increase in the surface resistance after postannealing at 600 °C.

All previous studies point to the importance of thermal history on the catalytic activity and stability. However, there has been a lack of systematic and comparative research to elucidate the main reasons behind it. Here, we investigated three LSC64 films prepared by PLD with very different thermal histories and thus different microstructures and morphologies; a low-temperature-grown film, a postannealed low-temperature-grown film, and last a high-temperature-grown film. We monitored how the microstructure/morphology, surface chemistry, local binding environment, and oxidation states of the low-temperature-grown film evolved with postannealing and how they were compared with the high-temperature-grown one. In this study, various elemental characterization techniques, that is, X-ray photoelectron spectroscopy (XPS), low energy ion scattering (LEIS) spectroscopy and secondary-ion mass spectrometry (SIMS) provide complementary information regarding the chemical restructuring of the films from the electrode/air to the electrode/electrolyte interface. These results were coupled with structural, microstructural, and electrochemical characterization techniques. Our results emphasize the importance of thermal history and processing of the SOC electrode films on the catalytic activity and stability and propose that they should be considered as among the main pillars in the design of active and stable surfaces.

2. EXPERIMENTAL SECTION

2.1. Thin Film Deposition. PLD targets were prepared from a commercial $La_{0.6}Sr_{0.4}CoO_{3-\delta}$ powder supplied by Praxair (99.9% purity). The average powder stoichiometry was analyzed by inductively coupled plasma−optical emission spectrometry (iCAP 6500 Thermo Scientific, USA), and the composition was found to be $La_{0.59\pm0.01}Sr_{0.41\pm0.01}Co_{1.00\pm0.01}O_{3-\delta}$, in good agreement with the nominal stoichiometry. Henceforth, this is referred to as $La_{0.6}Sr_{0.4}CoO_{3-\delta}$ or simply as LSC64. The LSC64 powder was pressed as 30 mm diameter discs using a uniaxial press, followed by consolidation in an isostatic press (350 MPa) and sintering at 1250 °C for 8 h in air.

The films were deposited using a Neocera PLD system (COMPex 205 F, Coherent) with a 248 nm KrF excimer laser with 25 ns pulse duration. During the experiments, the laser fluence was 0.1 J in 0.1 cm^2 spot size, while the laser repetition rate was 10 Hz. The target to substrate distance was set to 5 cm, while the target was rastered during the deposition process. Prior to the deposition, the chamber was evacuated to 6.6×10^{-6} mbar, and then the partial pressure of oxygen gas during deposition was increased to 0.043 mbar. The substrate temperature was varied between 100 and 750 °C for each deposition. In the rest of the article, the films deposited at 100 °C are referred to as low-temperature-grown or LT-grown, and those deposited at 750 °C as high-temperature-grown, or simply as HT-grown. The crystallization of LT-grown films was enhanced by annealing at 600 °C for 4 h in ambient air postdeposition, and they will be referred to as postannealed LT-grown films. As the density of the films increased with deposition temperature, the number of pulses was increased from 5000 (100 °C) to 5400 (750 °C) pulses to get similar thicknesses in all films (∼200 nm). After the deposition, the oxygen partial pressure in the chamber was increased to 800 mbar to oxidize the films *in situ*. Consequently, the temperature was reduced at a 20 °C min^{-1} rate to room temperature (RT) before the removal of the substrate. Single-side polished Si(001) substrates were used for structural and microstructural characterizations. For electrochemical characterization, polycrystalline 10% Gd-doped ceria (GDC) (Praxair, 99.9%) were used as substrates. The GDC substrates were polished using silicon carbide papers (P320/P500/P800/P1200/P2400/P4000) followed by subsequent diamond suspensions (9, 6, 3, 1, 1/4 μm). Film thicknesses after PLD deposition were measured using a Dektak 150 surface profiler.

2.2. Structural Characterization. Thin-film X-ray diffraction (XRD) characterization was performed in a four circle XRD Panalytical Empyrean diffractometer with Cu Kα radiation (line-focus). The data were collected in the $\theta/2\theta$ geometry with a scan range between 10 and 120° 2θ and a 0.02° step width with a 1 s step time. *In situ* XRD measurements were performed in a Panalytical Empyrean diffractometer with Cu Kα radiation up to 750 °C using an Anton Parr HTK1200N environmental heating chamber. The first measurement was taken at RT, and following measurements were taken between 400 and 750 °C at every 50 °C at a 10 °C min^{-1} heating rate for the films deposited on Si substrates. The data were collected in the $\theta/2\theta$ geometry with a scan range between 20 and 55°, a 0.03° step width and a 1 s step time. On GDC substrates, the measurements were performed between 450 and 750 °C at every 25 °C at a ramp rate of 10 °C min^{-1}. After the sample was cooled to RT, a final measurement was taken.

Raman spectroscopy was performed using a Renishaw Raman system equipped with a confocal microscope and a 20-mW argon laser (λ = 514 nm). 10% of the laser power and 10 s acquisition time were used in the measurements, and two scans were averaged over 20 × 20 μm^2 analysis area.

https://dx.doi.org/10.1021/acsami.0c08308
ACS Appl. Mater. Interfaces 2020, 12, 34388−34401

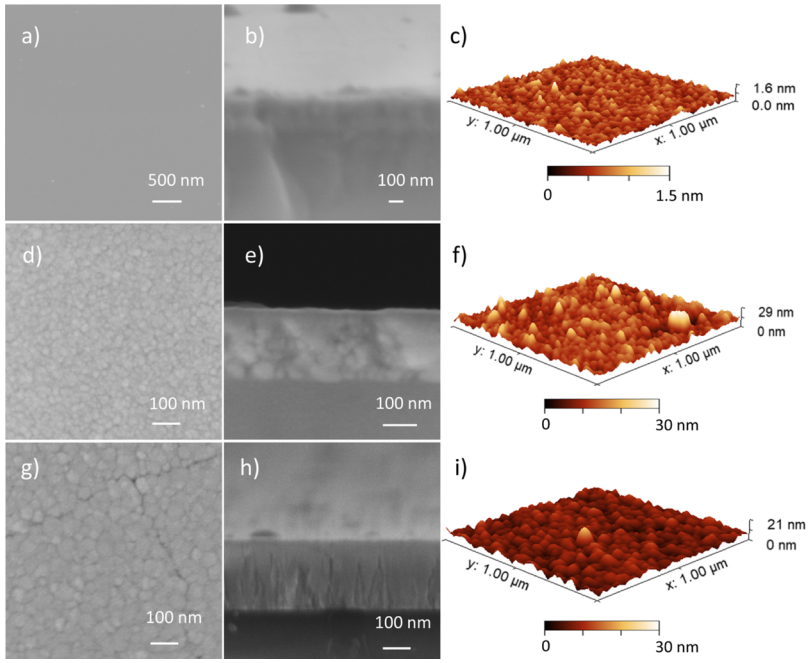

Figure 1. Top-view (a,d,g) and cross-section view (b,e,h) SEM micrographs and corresponding AFM images (c,f,i) showing the topography of LSC64 films deposited by the PLD on Si substrates: (a–c) LT-grown film, (d–f) postannealed LT-grown film, and (g–i) HT-grown film.

2.3. Microstructure and Morphology Characterization. The microstructure of the films was studied by scanning electron microscopy (SEM) using a Zeiss Auriga Cross microscope operating at an accelerating voltage of 5 kV and ~7 mm working distance. The films were coated with Cr to avoid surface charging. The surface morphology of the films was examined using an Asylum MFP-3D atomic force microscopy (AFM) instrument. AFM data were analyzed using open-source software Gwyddion 2.53.[25] The micrographs were taken on 1.0 × 1.0 μm^2 scan area using 512 × 512 px.

2.4. Electrochemical Characterization. The electrochemical characterization of the films was performed using a Solartron 1260 frequency response analyzer over the temperature range of 400–600 °C, and in the frequency range of 13 MHz to 0.1 Hz at an amplitude of 20 mV. All of the samples were measured at the open-circuit potential (OCP). The samples were contacted with Au grids (Goodfellow, 1500 wire/in.) and then sandwiched between Al_2O_3 blocks with gas channels, which were pressed to ensure maximum contact points. The impedance diagrams were fitted with electrical equivalent circuits using ZView 2 software (3.5f, Scribner Associates). The resistance multiplied with the geometric surface area of the electrodes and divided by two (symmetrical on the electrolyte) gave the area-specific polarization resistance.

2.5. Surface Characterization. The outermost atomic surface and subsurface chemical compositions were measured with a Qtac100 LEIS spectroscopy instrument (IONTOF GmbH, Münster, Germany) operated with normal incidence He^+ (3 keV) and Ne^+ (5 keV) as primary beam sources. The instrument is coupled with a secondary ion beam sputtering source of 1 keV Ar^+ incident at 45° to normal and provides information about the subsurface region. The LEIS depth profile analysis was run by alternating the analysis Ne^+ beam with the Ar^+ sputtering beam with a dwell time of 5 s. The primary beam scanning area was set as 1000 × 1000 μm^2 and the rastered area with the secondary ion beam was 1500 × 1500 μm^2. The rastered area was later analyzed with an optical surface profilometer (Zygo, NewView 9000). The analysis depth at an Ar^+ ion sputter density of 85 × 10^{15} atoms/cm^2 was approximately 18 nm.

Cation depth profiles in the films were analyzed using time-of-flight SIMS (ToF-SIMS) on a ToF-SIMS5 machine (IONTOF GmbH, Münster, Germany) equipped with a bismuth liquid metal ion gun. A 25 keV Bi^+ primary ion beam was used to generate secondary ions in the high current bunch mode and 10 keV argon cluster beam (Ar_n^+) was used for the depth profiling. Positive secondary ion species originating from the film and the substrate were monitored. Analysis area was 100 × 100 μm^2, and the sputtering area was 300 × 300 μm^2. After the experiments, approximately 300 nm analysis depth crater was measured by an optical surface profilometer.

The surface chemistry and electronic structure were characterized using a Thermo Fisher Scientific K-Alpha$^+$ XPS system operating at 2 × 10^{-9} mbar base pressure at ambient temperature. The system incorporates a 180° double focusing hemispherical analyzer with a 128-channel detector while the Al Kα X-ray source generates a 6 mA emission current with a spot size of 400 μm^2. Pass energies of 200, 20, and 15 eV were used for the survey, core-level spectra, and valence spectra, respectively. The spectra were taken at two emission angles, 0 and 70°, where the higher emission angles (70°) are more surface sensitive. The quantitative analyses were performed using Avantage software.[26] A Shirley background was subtracted from the data, and peaks were fitted using a convolution of Gaussian and Lorentzian peak shapes. Sr 3d, La 3d, Co 2p, O 1s, and C 1s spectra were analyzed at both emission angles. The spectra were normalized to the total integrated intensity of the La $3d_{5/2}$ spectra. The binding energies were corrected to the C 1s peak position at 284.8 eV originating from surface hydrocarbons. Prior to the experiments, the postannealed LT-grown and the HT-grown samples were heat-treated under dry oxygen gas flow at 250 °C for 30 min to remove the carbonaceous and hydrogenous species adsorbed on the surface. As the LT-grown film did not receive any heat-treatment previously, this procedure was omitted in order not to alter the surface.

2.6. Oxygen Ion Transport Kinetics. Oxygen self-diffusion and oxygen surface exchange kinetics of the films were obtained by isotopic labeling coupled with SIMS analysis. For ^{18}O isotope labeling, the samples were placed in a quartz tube, which was evacuated to <10^{-7} mbar. The exchange temperature was 400 °C. First, an exchange with 200 mbar of the ^{16}O atmosphere (99.9999%, ^{18}O natural abundance of 0.2%) was performed for 150 min to eliminate any oxygen defect related to the PLD deposition and to ensure the films reach thermodynamic equilibrium with the oxygen gas at the exchange temperature. Then, the films were exchanged in 200 mbar of the ^{18}O enriched atmosphere (90%) for 15 min. Partial pressure of 200 mbar was chosen to simulate the oxygen partial pressure at atmospheric pressure. The annealing time was corrected according to the real heating and cooling ramps using the Killoran

https://dx.doi.org/10.1021/acsami.0c08308
ACS Appl. Mater. Interfaces 2020, 12, 34388–34401

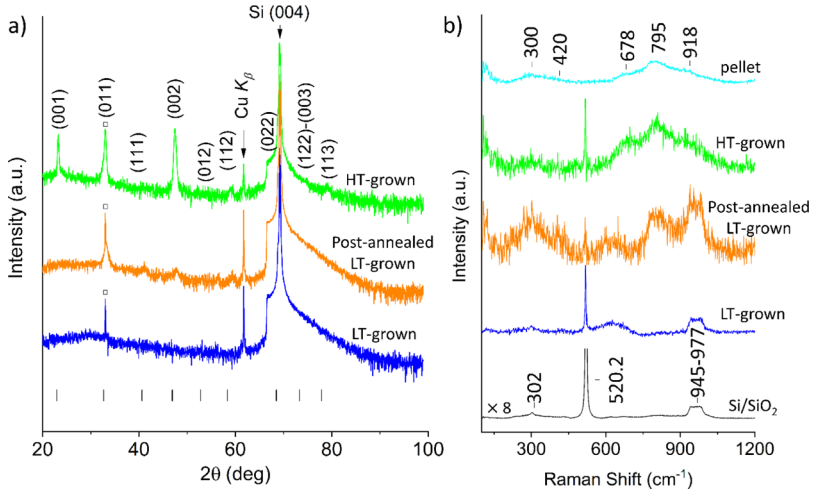

Figure 2. (a) XRD diffractograms of the LT-grown, postannealed LT-grown and HT-grown films deposited on the Si substrate. Vertical lines indicate the pseudocubic structure of LSC64 with a lattice parameter of 3.8741(3) Å. The peak indicated by the square is the Si(002) forbidden reflection. (b) Raman spectra of bare Si/SiO_2 (001), LSC64 pellet used as a PLD target and the films. The XRD plots are on a logarithmic scale, and spectra are shifted vertically in both figures. The intensity of the bare Si/SiO_2 in (b) was zoomed in for clarity. The peak positions in (b) are approximative.

method.[27] After 15 min of exchange, the samples were quenched to RT. Diffusion profiles were analyzed using ToF-SIMS. A 25 keV Bi^+ primary ion beam was used to generate secondary ions in the burst alignment mode (7 pulses) and 0.5 keV Cs^+ sputter beam was used for the depth profiling. Negative secondary ion species originating from the film ($^{18}O^-$, $^{16}O^-$, LaO^-, SrO^-, CoO) as well as the substrate (SiO^-, SiO_2^-) were monitored. Several films and analysis areas (20 × 20, 50 × 50, 100 × 100, and 300 × 300 μm^2) were investigated to check the reproducibility of the measurements. This is particularly important as the films might exhibit microstructural defects in the forms of cracks or porosities. Notably, special attention was devoted to the analysis of the HT-grown film as it exhibited cracks when deposited on Si substrates due to large lattice mismatch. The normalized ^{18}O diffusion profiles were fitted using the plane-sheet solution to the Fick's second law of diffusion equation to calculate oxygen self-diffusion coefficient (D^*) and surface exchange coefficient (k^*) using MATLAB app TraceX.[28]

3. RESULTS

3.1. Structural and Microstructural Characterization.

The microstructure and the surface topography of the LSC64 films were investigated by SEM and AFM. Figure 1 shows the SEM top-views and the cross-section views of the LT-grown, postannealed LT-grown, and HT-grown films deposited on oriented Si(001) substrates by PLD. From the SEM top-views (Figure 1a,d,g), the LT-grown film seemed to be quite flawless, dense and homogeneous, whereas the two other films had a granular appearance. The formation of cracks was observed in the HT-grown film (Figures 1g and S1c). They occurred after deposition on cooling (15 °C min^{-1} rate) and resulted from the differences in thermal expansion coefficients (TEC) between the film and the substrates (TEC; Si = 2.5 × 10^{-6} K^{-1},[29] LSC64 = 20.5 × 10^{-6} K^{-1},[30] and GDC = 14.4 × 10^{-6} K^{-1}[31]). The cracking in the postannealed film (Figures 1d and S1a,b) was avoided as the heating and cooling rates were set to 2 and 3 °C min^{-1}, respectively.

SEM cross-section views (Figure 1b,e,h) indicated that all films were similarly 200 ± 20 nm thick. The grains reached ~30 ± 10 nm size after postannealing of the LT-grown film at 600 °C for 4 h in ambient air, while an average grain size of ~60 ± 10 nm was observed in the as-deposited HT-grown film. The postannealed LT-grown film was observed to crystallize with randomly oriented grains, as expected for a homogeneous nucleation process. On the other hand, the HT-grown film showed columnar-type growth on the Si substrate in agreement with earlier PLD studies.[8,32] It is important to note that the films deposited on the polycrystalline GDC substrates for the electrochemical measurements followed similar nucleation and grain growth as those on the Si substrates (Figure S2).

Figure 1c,f,i show the surface topography of the films analyzed by AFM. The root mean square (rms) roughness of the films was found to be 0.15 ± 0.01 nm for the LT-grown film, 3.24 ± 0.1 nm for the postannealed film and 2.09 ± 0.1 nm for the HT-grown film. Particularly, the postannealed LT-grown film showed some protruding particles reaching up to ~30 nm from the surface (Figures S1 and S3). The HT-grown film had a lower roughness than the postannealed LT-grown film but also had a few particles reaching ~20 nm (Figure S3).

The crystallinity and crystal structure of the films grown on Si substrates are shown in Figure 2a. The polycrystalline PLD target XRD pattern can be assigned to a rhombohedral perovskite phase (Figure S4). The diffractogram of the LT-grown film only showed peaks corresponding to the substrate, suggesting that the film might be amorphous or have an extremely small crystallite size. After postannealing at 600 °C, the diffraction pattern was composed of at least five additional reflection lines, which matched well with a pseudocubic structure of the material. All peaks were rather broad, which could be attributed to a poorly crystallized or small grain size film. The HT-grown film diffraction pattern showed only three intense and narrow peaks corresponding to (001), (011), and (002) reflections compared with the postannealed film. Their intensity and low full width at half-maximum (fwhm) suggest a well-crystallized material with a larger grain size, agreeing with the SEM micrographs. Moreover, the texture along the (001) direction was observed not only on an epitaxial Si(001) substrate but also on the polycrystalline GDC substrate (Figure S5). In contrast, the postannealed LT-grown film was polycrystalline with no preferred orientation.

https://dx.doi.org/10.1021/acsami.0c08308
ACS Appl. Mater. Interfaces 2020, 12, 34388−34401

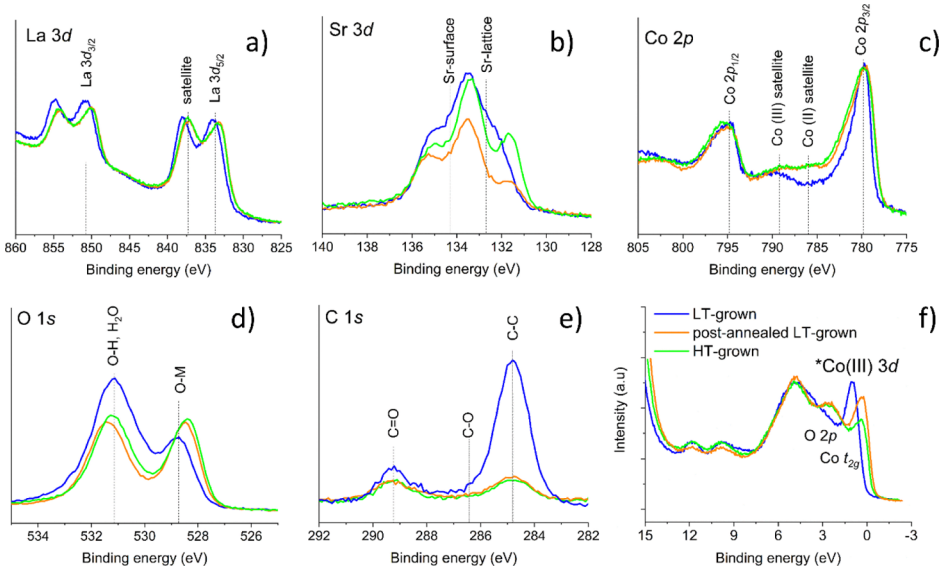

Figure 3. X-ray photoelectron spectra of La 3d (a), Sr 3d (b), Co 2p (c), O 1s (d), and C 1s (e) core-level spectra of the films measured at 70° emission angle. Main and satellite peak positions are indicated in each plot. (f) Showing valence band spectra. The spectra were normalized to the sum of the intensity.

The crystallization temperature of the LT-grown film on both substrates was also studied using *in situ* XRD measurements (Figure S6). The XRD patterns appeared at ~500 °C on both substrates, but with a much lower intensity on the GDC substrate. A new peak appeared at 43.7° at 700 °C and was retained after cooling down. It could originate from the formation of a new phase. For this reason, the electrochemical characterization was limited to an interval of 400−600 °C.

The XRD technique suggested that the LT-grown film might be either amorphous or composed of extremely small-sized crystallites. However, it is not possible to extract further detailed information from these patterns because of detection limits and peak broadening. From the literature, it is well-known that Raman spectroscopy is an efficient tool for the study of structural disorder in materials from Raman shifts and line shape evolution (broadening, intensity) of the Raman modes.[33] Therefore, to complement the XRD structural analyses, we performed Raman spectroscopy measurements at RT on the films as well as on the bare Si/SiO_2 substrate and LSC64 pellet to obtain reference spectra (Figure 2b). The substrate spectrum is composed of a sharp and very intense Raman line at approximately 520 cm^{-1} and many second-order lines, with the more intense ones occurring at 302 and 945−977 cm^{-1}. The Si signal of the substrate was subtracted from the spectra of the three films after normalization of the high intensity Si line in each spectrum to that in the bare Si substrate spectrum. Although some remaining substrate peaks were still observed, the Si subtraction made the peaks related to the films, if any, more visible.

The first-order Raman spectrum of ABO_3 rare earth perovskites, such as $LaCoO_3$, originates because of Jahn−Teller (J−T) distortions,[34,35] as no Raman-active mode exists for the ideal cubic perovskite structure. J−T distortions result in a structural disorder in the oxygen sublattice and particularly leads to differences in Co−O bond lengths in the CoO_6 octahedra,[36,37] changing the crystal structure locally from rhombohedral ($R\bar{3}c$) to monoclinic ($C2/c$). Such dynamical local site distortions may be associated with the intermediate spin state of Co^{3+}, which is strongly J−T active because of its partially filled e_g orbitals. Besides, an increase of the Sr content in doped $La_{1-x}Sr_xCoO_3$ led to a decrease in the intensity and peak broadening,[38] as similarly observed in $La_{1-x}Sr_xMnO_3$.[34] Therefore, line assignment becomes very difficult owing to the variability in the number and positions of lines in the spectra. The Raman spectrum of rhombohedral distorted perovskites (space group, $R\bar{3}c$) is expected to be composed of five active modes ($A_{1g} + 4E_g$). In the literature, very few papers deal with Raman studies of $LaCoO_3$ and related $La_{1-x}Sr_xCoO_3$ perovskites; the following ones illustrate this variability. Ishikawa *et al.* reported Raman modes of $LaCoO_3$ single crystals at 61 (E_g), 160 (E_g), 425 (E_g), 230 (A_{1g}), 536, and 653 cm^{-1} (two broad peaks enhanced by J−T distortions), whereas only the first three were observed in $La_{0.7}Sr_{0.3}CoO_3$ because of its metallic state.[38] In the Raman study of polycrystalline $LaCoO_3$ samples (2−4 μm grain size), Orlovskaya *et al.* reported only four Raman active modes at 162, 448, 557, and 673 cm^{-1}.[35] Raman lines for nanocrystalline $LaCoO_3$ (5.6 nm grain size) and $La_{0.8}Sr_{0.2}CoO_3$ (LSC82, 11.5 nm grain size) by Li *et al.* were reported at 130, 305, 420, 570, 700, 810 cm^{-1} and at 305, 500, 630, 812, 910 cm^{-1}, respectively.[39] In our study, the spectrum of the LSC64 dense pellet showed Raman bands at approximately 300, 420, 678, 795, and 918 cm^{-1}. Knowing that these positions were rather approximate because of the broadness and low intensity of the lines, we can consider a good correspondence with the line positions of LSC82 in ref 39.

Regarding our films, the spectrum of the LT-grown film was very similar to the bare Si/SiO_2 substrate without any line of the LSC64 crystalline pellet; therefore, it suggests an amorphous film. In contrast, the significant similarity between the HT-grown film and the pellet spectra indicates that the film is well-crystallized and has the rhombohedral structure of the LSC64 pellet locally. The Si second-order lines were not visible, probably because of a difference in the laser penetration depth in the amorphous and crystalline films related to their different transparencies (or absorption). In contrast, Si second-order lines were still visible in the postannealed film as well as an additional broad band at approximately 810 cm^{-1}, that is, at

https://dx.doi.org/10.1021/acsami.0c08308
ACS Appl. Mater. Interfaces 2020, 12, 34388−34401

a position very close to the one at 795 cm^{-1} in the spectrum of the pellet sample. Therefore, this spectrum suggests that the film is partly but not fully crystallized.

3.2. Oxidation State, Local Binding Environment, and Chemical Quantification by XPS. The defect structure of LSC64 has been well-documented in the literature.[40] Substitution of La^{3+} with a lower oxidation state cation such as Sr^{2+} must be charge compensated with an equivalent positive charge. This could be achieved with either the oxidation of cobalt from Co^{3+} to Co^{4+} ($Co_{Co}^{\bullet}$) and/or the creation of oxygen vacancies ($V_O^{\bullet\bullet}$). The reduction of Co^{3+} to Co^{2+} may result in creating more oxygen vacancies to compensate for the negative charge.

Some previous studies showed a correlation between the increased concentration of oxygen vacancies ($V_O^{\bullet\bullet}$) at the surface and the Sr segregation. It is induced by the electrostatic attraction of the oxygen vacancies with the negatively charged A-site dopants (Sr_{La}') toward the surface and thus leading to a faster deterioration of the electrodes.[41,42] Therefore, XPS analyses were performed to compare the chemical composition and the chemical environments (or oxidation states) of elements of interest in all the samples.

Figure 3 shows La 3d, Sr 3d, Co 2p, O 1s, and C 1s core-level spectra measured at a 70° emission angle, as the spectra collected at higher angles more reflect the surface chemistry. The survey spectra (Figure S7) showed no surface contamination. O 1s and C 1s spectra of the LT-grown film showed different levels of adventitious carbon (284.8 eV) and other weakly adsorbed surface species OH− and H_2O (around 531 eV) (Figure 3d,e). This is because the film was measured as-deposited without further cleaning procedure. O 1s core-level peaks show two peaks at around 531 and 528.6 eV. The peak at a higher binding energy of ∼531 eV may be assigned to weakly adsorbed species at the surface (OH^-, H_2O, C−O, C═O *etc.*), while the peak at lower binding energy ∼528.6 eV is characteristic of metal−oxygen bonding in the crystal network.[43]

XPS analyses suggest that the LT-grown film had a slightly different coordination and binding environment than the other two films. On the other hand, different crystallization kinetics in the postannealed LT-grown and HT-grown films induced slight variations in the surface and defect chemistry. The major difference between the two crystalline films was observed in the Sr 3d and Co 2p core-level spectra, indicating a cause and effect relation, that is, a change in the surface-bound Sr concentration result in the change in the average Co-oxidation state.[19]

Analysis of the spectra shown in Figure 3b provides information on the amount and the nature of Sr segregated toward the surface. The Sr 3d photoelectron spectrum consists of a doublet with $3d_{5/2}$ at lower binding energies (131.6 ± 0.2 eV) corresponding to the lattice-bound Sr and $3d_{3/2}$ at higher binding energies (133.3 ± 0.2 eV) corresponding to the surface-bound Sr (see Figure S8 for peak fitting). Figure 4a shows the Sr/A-site ratio analyzed at different emission angles by XPS (0 and 70°). Analyses at both angles show that the amount of lattice-bound Sr was lower than expected (0.4) for all samples, and it decreased further near the surface. The overall trend was more pronounced in the postannealed sample. Figure 4b shows the Sr-surface sites to the sum of all Sr sites (surface-bound and lattice-bound). The postannealed film again showed higher values than the other two films, suggesting higher amounts of strontium-based particles such

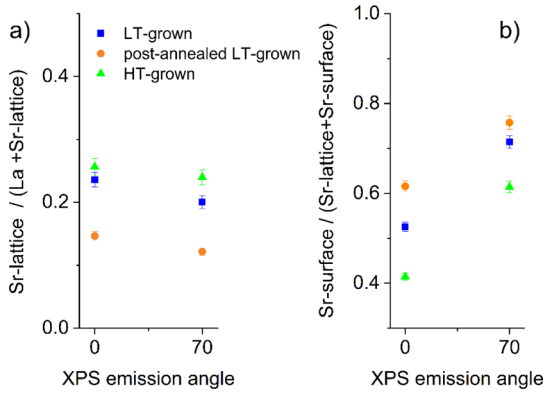

Figure 4. (a) Ratio of Sr lattice to the A-site (sum of La and Sr-lattice), and (b) ratio of Sr-surface sites to the sum of all Sr sites (surface-bound and lattice-bound) deduced from XPS measurements at two emission angles.

as carbonates; $SrCO_3$, hydroxides; $Sr(OH)_2$, oxides; SrO at the surface. Deposition temperature,[19] annealing temperature and dwell time,[18] strain in thin films[44] as well as the annealing atmosphere and microstructure[45,46] were shown to influence the Sr segregation behavior in similar perovskites.

Focusing on the Co 2p core-level (Figure 3c), it can be seen that the spectra are split into two parts because of the spin−orbit coupling: $2p_{1/2}$ and $2p_{3/2}$, where each one has a main and satellite peaks. Although Co^{3+} and Co^{4+} peaks are indistinguishable, the separation between the main peaks and the satellite peaks are considered useful to survey the +2 and +3 oxidation states.[19,47,48] The higher binding energy satellite peak (∼789 eV) was attributed to the +3 oxidation state, while the lower binding energy peak (∼786 eV) was assigned to +2. The LT-grown film showed mainly Co^{3+} peak, while both the postannealed and the HT-grown films showed a mixture of +2/+3. Furthermore, the fwhm of the Co $2p_{3/2}$ peak of the HT-grown sample (3.1 eV) was larger than the others (2.89 and 2.22 eV for postannealed and LT-grown, respectively), suggesting more Co^{2+} in the HT-grown film.

Next, the valence band spectra are compared and shown in Figure 3f. The peak near the Fermi level arises from the hybridization of Co t_{2g} and O 2p bands, and the peak intensity provides information on the Co-oxidation states.[49] As expected, the spectra are very different between the amorphous and the crystalline films. Postannealed LT-grown and HT-grown films show a metal-like Fermi edge (E_f).[50] The higher intensity of the valence band edge indicates a higher amount of Co^{3+}. Therefore, the Co^{3+} concentration goes in the order of LT-grown > postannealed LT-grown > HT-grown film, similar to the observations in Figure 3c. It is important to note that previous reports observed the oxidation of Co^{2+} to Co^{3+} simultaneously with the segregated Sr-based species, and this behavior was attributed to the degradation of the LSC64 surfaces.[19]

Tables S1−S3 show the % atomic composition, peak binding energies, and fwhm of the fits at two emission angles. In general, the A-site elemental content was found to be higher than the B-site for all films. Similar results were found both on powder[43] and thin-film LSC64[19] samples. It is important to note that these results are an integration over a thickness defined by the energy of the photoelectrons and the angle of incidence. Therefore, the difference of inelastic mean free path of elements may have an influence on the sampling depths of

https://dx.doi.org/10.1021/acsami.0c08308
ACS Appl. Mater. Interfaces 2020, 12, 34388−34401

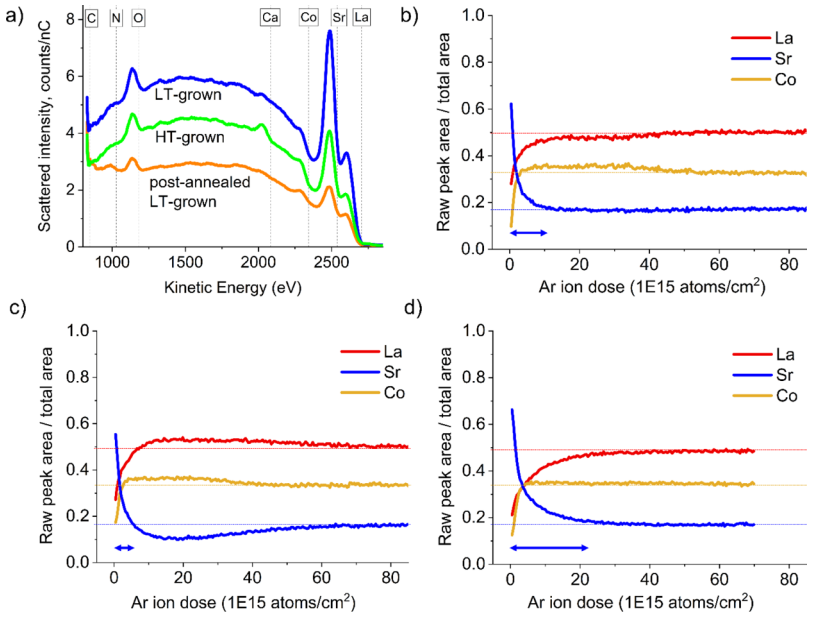

Figure 5. (a) LEIS survey spectrum showing the outermost surface composition of the LSC64 films. The data were measured with 3 keV He^+ primary beam. Depth profiling analyses were performed with 5 keV Ne^+ primary beam and 1 keV Ar^+ sputtering beam, corresponding to (b) LT-grown, (c) post-annealed LT-grown, and (d) HT-grown films. The blue arrows indicate the depth of Sr-rich regions in the films.

photoelectrons depending on the kinetic energy. From the Tables S1−S3, atomic percentage of all elements decrease toward the surface, except for the surface-bound Sr and surface-bound O related to the secondary phases and/or adsorbates.

Considering La 3d/Sr 3d (sum of all Sr sites) peak ratios at 0° emission angle gave ∼0.61:0.39, ∼0.69:0.31 and ∼0.63:0.37 for the LT-grown, postannealed LT-grown and HT-grown samples, respectively. It suggests that close to stoichiometric bulk values were obtained in the as-deposited LT- and HT-grown films. On the other hand, postannealing seemed to change the average La/Sr ratio, by increasing La and decreasing Sr in the probed area. In the next section, this behavior will be investigated by LEIS, which provides chemical depth profiling with layer-by-layer atomic resolution.

3.3. Outermost Surface Composition and Chemical Depth Profiling by LEIS. LEIS analysis was used to survey the outermost elemental cation composition. However, coupled with a sputter beam, it can also give depth profile information. In previous literature reports, LEIS depth profiles were normalized to the stoichiometry of the bulk, assuming the cation concentration that has reached a plateau a few nanometers below the surface to be representative of the bulk concentrations.[21,24,51] In this work, elemental quantification has not been attempted because depth profiles may display preferential sputtering for heavier elements such as La.[52] Therefore, depth profiles in this work provide qualitative information and is used only to compare the surface chemical evolution among the three films.

Figure 5 shows the LEIS surface survey spectra and depth profiling of LT-grown, postannealed LT-grown, and the HT-grown films, respectively. The background-corrected raw peak area for La, Sr, and Co (fitted with a Gaussian profile) divided to the total peak area is expected to provide a true variation of the chemical restructuring among the three films. Moreover, as the analysis area and the acquisition dose were kept constant during the measurements for each sample, the analyses depth and the cation ratios could be comparable. The *x*-scale in the depth profiles in Figure 5b−d show the sputtering Ar^+ ion dose, in which, increased values give chemical composition information from the subsurface. Horizontal lines with the same color of each element were added as a guide to the eye, and they indicate the approximate bulk composition, deduced from the steady data points at high Ar^+ ion dose.

Sr enrichment was evidenced for all the investigated films, including the LT-grown film, at the outermost-surface layer (Figures 5a and S9). At the same time, La and Co seemed to be depleted at the surface (Figure 5a) and a few atomic layers below the surface (Figure 5b−d). Similar behavior was observed with other Sr-containing perovskites.[19] A pronounced difference between the films was observed in the near-surface, as shown in the depth profiles. Notably, a region with highly depleted Sr and increased La concentration appeared a few nanometers below the surface of the postannealed LT-grown film. As a reminder, a similarly high ∼La/Sr ratio was found in the postannealed LT-grown film by XPS. It is important to note that coupled with a sputter beam LEIS probed a volume much deeper than XPS. Ar^+ sputter dose at 85×10^{15} atoms/cm^2 as in Figure 5b−d corresponds to ∼18 nm below the surface, whereas, XPS probes typically ∼5−10 nm. Moreover, chemical concentrations are averaged over the whole analysis volume in XPS. Thus, LEIS depth profiles show that, at a similar depth probed by XPS, the ∼La/Sr ratio already reached stoichiometry in LT- and HT-grown films, while it remained still high in the postannealed LT-grown film. Therefore, LEIS successfully demonstrated the layer-by-layer evolution of chemical concentrations in all films until the bulk concentration has been reached.

The evolution of chemical concentration is particularly interesting considering the microstructural differences between the postannealed LT-grown and the HT-grown films. The postannealed film showed a higher density of grains (∼30 nm) at the surface compared with the HT-grown film (∼60 nm). Notably in the postannealed LT-grown film, the segregation

https://dx.doi.org/10.1021/acsami.0c08308
ACS Appl. Mater. Interfaces 2020, 12, 34388−34401

appeared to enhance in the vicinity of the surface (where Sr became deficient). On the other hand, the HT-grown film showed a three-times thicker Sr-rich subsurface region (indicated with the blue arrows in Figure 5b–d). As the HT-grown film possesses a vertically ordered columnar microstructure, Sr could segregate increasingly and homogeneously to the surface through the grain boundaries.[20]

It is important to note that the chemical composition in the analyzed depth cannot be compared directly between the three films. For instance, an average of 18 nm depth in the LT-grown film (rms: 0.15 ± 0.01 nm) corresponds to an analysis area, which is uniform and flat below the surface, whereas the analysis depth of the postannealed LT-grown (3.24 ± 0.1 nm) and HT-grown film (2.09 ± 0.1 nm) follows the rough and granular surface.

In summary, XPS is known to be free of matrix effects and provide quantification, oxidation states, and information about the binding environment. However, the depth information remains limited to a few nanometers below the surface. Although XPS can also be coupled with a sputter gun to give depth information, LEIS is capable of providing chemical resolution at the atomic scale. Besides, LEIS is sensitive to the first atomic layer. In Section 3.6, the SIMS technique will be used to investigate the elemental distribution in the long-term annealed samples used in electrochemical measurements.

3.4. Oxygen Self-Diffusion and Surface Exchange Kinetics by IEDP–SIMS. The oxygen self-diffusion coefficient (D^*) and surface exchange coefficient (k^*) of a material is used as a measure of catalytic activity. Figure 6 shows the D^*

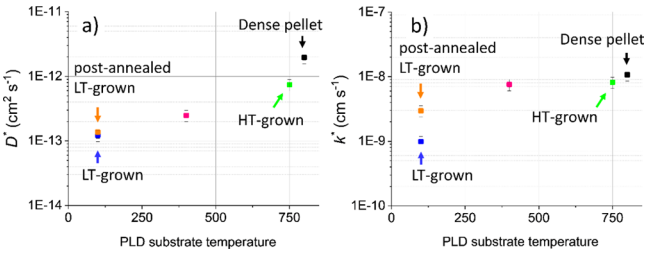

Figure 6. D^* and k^* values measured for ~200 nm thick LSC64 films that have been isotopically exchanged in an $^{18}O_2$ enriched atmosphere under the same conditions (T = 400 °C, anneal time = 15 min). The reference value was from a dense ceramic pellet sintered at 1200 °C.[53]

and k^* values of the films deposited at various $T_{substrate}$ (refer to Figure S11 for the fits). The isotopic exchange temperature was performed at 400 °C (15 min and at 200 mbar), as previous work reported enhanced D^* and k^* coefficients for low-temperature operation on LSC82 films grown at low $T_{substrate}$.[24] The values for a dense LSC64 polycrystalline ceramic pellet similarly exchanged at 400 °C for 15 min and at 230 mbar $O_{2(g)}$ were added for comparison.[53] It is important to consider the error from such short isotopic exchange time and low temperature. Because of slow equilibration time, it is difficult to extract the accurate D^* and k^* coefficients. Moreover, there might be another error source from the microstructural defects in the forms of cracks or porosities. It is also important to note that a preanneal of 150 min was performed at 400 °C prior to the exchange experiments. This is a relatively low-temperature treatment and a short time, therefore a substantial change in the surface composition or the morphology of the films is not expected. At the moment, the extent of each error source is not known, but an error bar of 20% has been included in Figure 6. Additionally, we performed several screening tests on the samples, and values from two locations with similar analysis conditions were reported in Table S4. The small standard deviation of the two measurement points for each sample indicate the compositional homogeneity of the films. On an interesting note, the isotopic fraction diffusion profile of the postannealed LT-grown film bears traces of higher surface contamination compared with the other two films (Figure S11b).

The D^* and k^* coefficients of the highly crystalline HT-grown film represented the closest match to those of a dense pellet sample. However, the LT-grown film showed an order of magnitude decrease in both values. After postannealing the LT-grown film, the k^* appeared to increase, but D^* did not improve. This might be due to the differences in the microstructures and crystallinity, as discussed in the Section 3.1.

This study provides evidence that thermal history and processing affect not only the microstructure and surface chemical concentration but also the oxygen transport kinetics. These results reflect that LSC64 films grown at low $T_{substrate}$ (*e.g.*, <500 °C) do not seem to provide an advantage for low-temperature SOC operation over films grown at high $T_{substrate}$ (>600 °C).

3.5. Electrochemical Characterization by Electrochemical Impedance Spectroscopy. In this section, the ORR activity and the stability of the films are assessed by electrochemical impedance spectroscopy (EIS) on symmetrical cells with the GDC electrolyte. It is noteworthy to mention that during the symmetrical cell preparation, one side of the HT-grown film underwent an additional high-temperature heat treatment during the preparation of the symmetrical cells, undoubtedly affecting the thermal history. However, the crystal structure and grain size of the sample remained similar on each side. Nevertheless, a change in the degradation mechanism, that is, on the activation energy and degradation rate, is not expected because both sides of the sample were prepared at the same temperature, but one side of the cell remained at this temperature for a slightly longer period. Figure 7 shows the Nyquist and Bode plots of LT-grown and HT-grown films

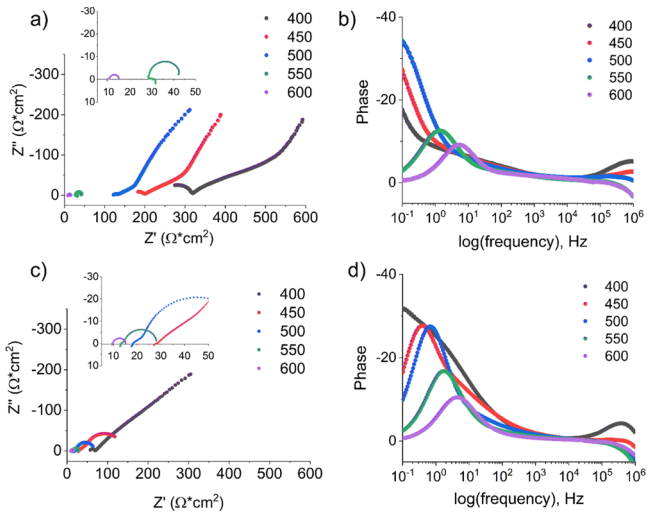

Figure 7. Nyquist and Bode plots of (a,b) LT-grown and (c,d) HT-grown films measured from 400 to 600 °C in OCP and ambient air. A dwell time of 1 h was set between the measurements.

https://dx.doi.org/10.1021/acsami.0c08308
ACS Appl. Mater. Interfaces 2020, 12, 34388–34401

measured on heating between 400 and 600 °C. The LT-grown film crystallizes *in situ* during the measurements; therefore, it becomes the postannealed film after reaching 600 °C.

Looking at the Nyquist plots between 400 and 500 °C (Figure 7a,c), much higher resistance values can be observed for the LT-grown film. The Bode plots demonstrated that the maximum frequency in the low-frequency arc of the LT-grown film was not obtained between 400 and 500 °C (Figure 7b). This was the case only at 400 °C for the HT-grown film (Figure 7d). The inset in Figure 7a shows that the spectrum was not in equilibrium at 550 °C, possibly because of the ongoing crystallization, but similar resistance values began to appear for both films. For these reasons, the impedance spectra of the LT-grown film were not fitted below 600 °C on the first heating cycle.

The high resistance values of the LT-grown film at low-temperature operations (*e.g.*, <500 °C) are in line with the isotope exchange measurements at 400 °C, meaning the LT-grown film does not provide an improvement for low-temperature SOC operation. However, after crystallization at 600 °C, the total resistance of the LT-grown film becomes comparable to that of the HT-grown film (Figure S12). Nevertheless, the Nyquist plot as shown in Figure S12 also points to a substantial difference among the contributing resistive components in these films.

Previous studies showed enhancements in the ORR kinetics at 600 °C for other LT-grown LSC64 films.[16,18,19] However, we would like to point out that the films in those reports were deposited on epitaxial YSZ(001) substrates and under 10-times higher oxygen partial pressures (*i.e.*, 0.4 mbar) than our work, suggesting a significant effect of processing on oxygen reduction and incorporation.

Next, temperature-cycling behavior was monitored between 400 and 600 °C (Figure 8a,b). The Arrhenius plots only show the values measured between 500 and 600 °C because below this temperature, the circuit model did not yield good fitting.

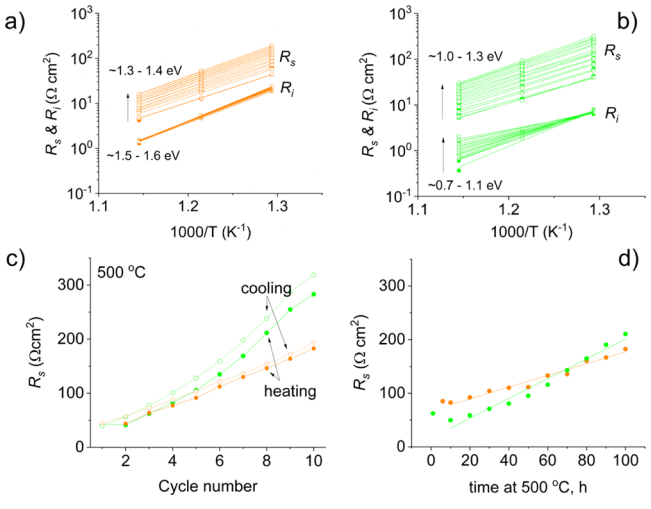

Figure 8. Arrhenius plots showing the degradation behavior of R_s and R_i on heating and cooling (10 cycles) between 500 and 600 °C; (a) LT-grown film (became the postannealed LT-grown film after the first heating cycle), (b) HT-grown film. (c) Stability of R_s at 500 °C during 10 consecutive heating and cooling cycles (between 400 and 600 °C), (d) stability of R_s at a fixed temperature (500 °C for ∼100 h). The orange signs refer to the postannealed LT-grown film, and green to the HT-grown film.

At least two resistive contributions are visible in the impedance plots. The resistance at the high-frequency arc (10^4 to 10^1 Hz) was attributed to the interfacial charge transfer resistance (denoted as R_i) and the low-frequency arc (10^1 to 10^{-1} Hz) to the surface resistance of the electrodes (denoted as R_s) (Figure S13).

Concerning R_i, the LT-grown film gave higher but stable values compared to the HT-grown film. On the other hand, the HT-grown film degraded at a much faster rate at 600 °C and exceeded the values measured for the LT-grown film. On the other hand, R_s initially gave similar values for both films, but the HT-grown film again degraded at a faster rate than the LT-grown film at all temperatures. Figure 8c focuses on the R_s values at 500 °C in Figure 8a,b during the 10 heating and cooling cycles. In the beginning, both films showed similar catalytic activity, but the HT-grown film began to degrade at a much faster rate. Higher R_s values were observed on cooling for both films, but again it was more pronounced on the HT-grown film.

Figure 8d shows the R_s values for the symmetrical LT- and HT-grown films at 500 °C at OCP for ∼100 h. After reaching 500 °C, impedance plots were collected after a 1 h dwell period. The LT-grown film crystallized *in situ* during the measurements (Figure S14). The degradation rate of the R_s component of the HT-grown film (∼2.40%/h) was found to be ∼2 times greater than the LT-grown film (1.12%/h). Taking into account all results from Figure 8, the LT-grown film appears to be more advantageous for its stability for long-term operation either on heating−cooling cycles or at a fixed operating temperature.

3.6. Chemical Depth Profiling by SIMS and LEIS after Long-Term Annealing at 500 °C. After long-term stability tests at 500 °C, we aimed to investigate the compositional changes at the solid/solid and solid/air interfaces. To this end, the SIMS instrument was used to monitor the positive secondary ions species originating from both the films and the substrate (GDC). The SIMS technique was chosen because of its good lateral resolution and fast analysis time. Also, investigations at the LSC64/GDC interfaces were found to be challenging because of the charge accumulation at the interface. This problem was eliminated using argon cluster sputter beam (Ar_n^+) as it was shown to be effective in compensating for the charge accumulation at the interface of oxide thin films and insulating substrates.[54] In addition, LEIS was used on long-term annealed films grown on Si substrates to monitor the outermost surface to near-surface compositional changes.

Figure 9a,b shows the SIMS depth profiles, where the normalized intensity (secondary cation signal divided by the total counts) is plotted against the sputter ion dose density. Particularly, the differential Sr^+ profiles are quite different. As seen in Figure 9a, an obtrusive trend was observed for the distribution of Sr, which extends to the whole thickness of the film. The HT-grown film as in Figure 9b shows a more uniform Sr^+ distribution except for the near-surface region, where a prominently higher SrO^+ signal is also visible.

Additionally, a cation interdiffusion layer (indicated with black dotted lines) can be observed for both samples at the interface. This layer was slightly thicker in the postannealed LT-grown film compared with the HT-grown film. Moreover, Sr^+ signal seemed to increase and make a longer tail at the electrode/electrolyte interface. These phenomena might help to explain the higher interfacial charge transfer resistance

https://dx.doi.org/10.1021/acsami.0c08308
ACS Appl. Mater. Interfaces 2020, 12, 34388−34401

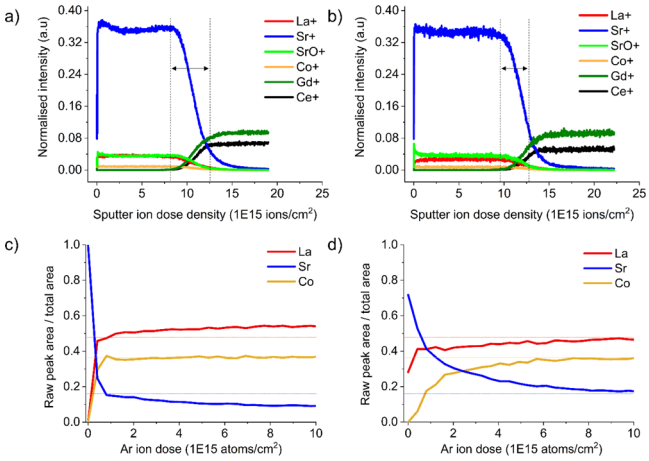

Figure 9. SIMS analyses of (a) postannealed LT-grown and (b) HT-grown films analyzed in the EIS during stability tests at 500 °C for 100 h. LEIS chemical depth profiling of (c) postannealed LT-grown and (d) HT-grown films grown on Si substrates, annealed similarly at 500 °C for 100 h. Horizontal lines in the LEIS spectra indicate the bulk stoichiometry values.

observed in the electrochemical characterizations of the postannealed LT-grown film.

To further investigate the surface region after long-term annealing, LEIS was used. Figure 9c,d shows the chemical distribution at the near-surface region (~2−3 nm) (refer to Figure S10 for an analysis crater similar to those of Figure 5). First of all, the outermost surface of the postannealed LT-grown film was entirely covered with a monolayer of Sr-based species, which is commonly observed after annealing.[55] However, just below this monolayer, Co concentration substantially increased and reached its bulk stoichiometry. This is probably related to the clustering of Sr precipitates into protruding particles, whereby the remaining surface could expose Co cations.

On the other hand, the HT-grown film showed a mixed La- and Sr-based monolayer termination. Below the outermost surface layer, Sr remained in excess, while Co remained deficient. Herein, we would like to draw attention to a recent study on a similar HT-grown LSC64 film.[56] The study observed the new growth of La containing SrO species at operation temperatures above 400 °C using an *in situ* near-ambient pressure XPS. Most interestingly, the new species preferentially grew on the electrochemically active Co sites. This is in agreement with our observations by LEIS analyses before and after annealing at 500 °C for 100 h.

The gradual disappearance of Co at the surface/subsurface with annealing might influence the ORR kinetics. Recent works based on first-principle calculations revealed that B-site termination (*i.e.*, CoO^{-}) provided faster O_2 dissociation than Sr-rich termination in $(LaSr)BO_3$ perovskites (B: Co, Mn, *etc.*).[57,58] Moreover, real-time impedance monitoring showed that Co decoration on SrO-coated deactivated LSC64 surfaces could still improve the catalytic activity.[59] Our recent work on $CoFeO_x$ (B-site) precipitation in the A-site deficient $(La_{0.7}Sr_{0.3})_{0.95}Co_{0.2}Fe_{0.8}O_3$ (LSCF) showed that nanoscale B-site oxides decorated the surfaces of LSCF, and thus lead to increased catalytic activity for ORR.[7]

Aside from the observed deactivation of the surfaces by A-site cation termination, thin layers of A-site oxide terminations must have sufficient ionic and electronic conductivity at the operating conditions of SOFCs.[60] On this matter, detailed density functional theory studies on SrO-terminated $SrTiO_3$ (STO) and Fe-substituted STO have revealed that SrO-terminated surfaces can actively participate in the molecular oxygen dissociation.[61,62] This was possible by creating electron-rich surface sites through oxygen vacancies with iron substitution in STO. In line with these results, our investigations confirm that the elemental distribution at the subsurface must be among the defining factors for the catalytic activity and stability of the electrodes.

4. DISCUSSIONS

Our motivation in this paper was to establish the factors that were influenced by the thermal history and processing of thin films. The sketch in Figure 10 takes into account the differences in the microstructures, morphologies, and the grain sizes of postannealed LT-grown and HT-grown films and depicts the surface restructuring after long-term annealing.

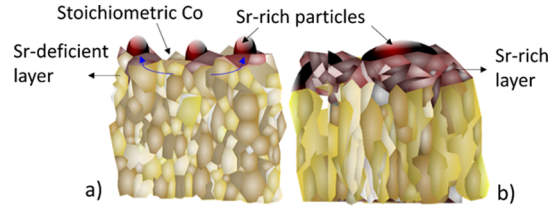

Figure 10. Surface restructuring of (a) postannealed LT-grown and (b) HT-grown films after long-term annealing at 500 °C.

A high density of grains resulting from two times smaller grain size on the surface of the postannealed LT-grown film has led to increased amounts of Sr precipitates. It appears that the Sr segregated locally from a few nanometers below the surface into the protruding particles at the surface. Local Sr segregation into clusters of Sr precipitates created a Sr-deficient region of several nanometers thick below the surface. At the same time, Co was exposed on the remaining surface and reached its bulk stoichiometry. In the HT-grown film, because of vertically aligned grains and grain boundaries, Sr could segregate from much deeper regions.[20] According to the LEIS analyses, the HT-grown film did not show a substantial Sr-deficiency in the subsurface as observed in the postannealed LT-grown film. Instead, the columnar microstructure facilitates the formation of a homogeneously covered Sr-rich layer on the surface.

Microstructural differences might also explain the behavior observed for the oxygen ion transport kinetics measured at 400 °C. The randomly oriented granular microstructure of the postannealed film could be impeding the direct diffusion of oxygen ions, whereas, oriented columnar microstructure along the diffusion path could be facilitating the oxygen diffusion in the HT-grown film. At higher temperatures, the surface elemental rearrangement helps to enhance the catalytic activity and the stability of the postannealed LT-grown film.

In relation to our observations, several reports have suggested that microstructure, grain size, and grain orientation might be responsible for the different Sr segregation behavior. Notably, Téllez *et al.* observed faster Sr segregation on LSC64 ceramic samples with a decrease of grain size after annealing for 1 h at 600 °C in dry oxygen.[63] Pişkin *et al.* showed that LSC64 ceramic sample with {001} grain orientation had more than 3 times higher area coverage than other orientations;

https://dx.doi.org/10.1021/acsami.0c08308
ACS Appl. Mater. Interfaces 2020, 12, 34388−34401

{101} and {111}.[64] As a reminder, our HT-grown LSC64 thin film showed a pronounced texture along the (001) direction. Therefore, apart from the obvious differences in the microstructure and grain size, the grain orientation may also be among the factors affecting the elemental distribution on the surface, in turn, the long-term stability of the films.

Previously, a few reports have investigated the effect of grain orientation on ion exchange and diffusion kinetics, but no universal conclusion was reached. For instance, Fearn *et al.* found no differences in D^* and k^* values in perovskite $La_{0.8}Sr_{0.2}MnO_3$ pellets.[65] On the other hand, Burriel *et al.* showed a fourfold difference in the D^* among the anisotropic $PrBaCo_2O_{5+\delta}$ polycrystalline grains.[66] In $La_2NiO_{4\pm\delta}$ thin films, ~2-orders of magnitude increase was observed along the (*ab*-plane) compared with (*c*-axis) orientated ones.[67] On the contrary; later studies reported similar k^* values regardless of the grain orientation.[68,69] It was suggested that the k^* was largely affected by the thermal history of the sample, the presence of impurities and surface rearrangement processes. Therefore, all these factors override any effect of grain orientation. This observation was also confirmed by a recent study, which investigated LSCF thin films deposited on GDC-buffered YSZ single crystal substrates having (100) and (111) orientations.[70] The films grown on (111) GDC/YSZ showed initially higher k^* compared to those grown on (100) GDC/YSZ. However, the former exhibited a higher degradation rate due to faster Sr segregation at the surface.

Finally, we have shown how the chemical reconstruction at the solid/solid and solid/air interfaces was affected by the thermal history and processing of thin films using a multitude of elemental characterization techniques (XPS, LEIS, SIMS). Although none of these techniques could perform point analysis because of detection limitations, we were able to propose a chemical restructuring scheme by combining all results from elemental characterisations while considering the microstructural and morphological features and the electrochemical performance of the films.

5. CONCLUSIONS

In this study, the influence of thermal history on the microstructure, elemental distribution from the air/solid to solid/solid interfaces, and consequently on the catalytic activity and stability of thin films were studied. Three $La_{0.6}Sr_{0.4}CoO_{3-\delta}$ (LSC64) thin films deposited by PLD were systematically examined. The film grown at $T_{substrate}$ = 100 °C (LT-grown) showed a quite flat and homogeneous morphology. After postannealing at 600 °C in ambient air, a disordered grain growth (~30 nm) and the formation of protruding particles were observed, whereas the film grown at $T_{substrate}$ = 750 °C (HT-grown) showed a textured columnar grain growth with ~60 nm grain size. The oxygen transport parameters of the LT-grown film were found to be up to an order of magnitude lower than the HT-grown film at 400 °C, suggesting that the HT-grown LSC64 films were more advantageous for low-temperature SOC operation. After postannealing at 600 °C, the ORR activity of the LT-grown film became comparable to the HT-grown one. Moreover, it showed a twotimes lower degradation rate in comparison to the HT-grown film. Both XPS and LEIS indicated a Sr-deficient region below the surface for the postannealed film. As the protruding particles were observed after the thermal treatments, it is believed that they might be linked with the localized and preferentially segregated Sr-rich particles. On the other hand, the HT-grown film showed a homogeneously distributed Sr-rich region compared with the postannealed LT-grown film. The columnar microstructure of the HT-grown film possibly facilitates the Sr diffusion through the grain boundaries toward the surface and thereby homogeneously covering the surface with a Sr-rich phase. This is believed to be the reason for its higher degradation rate at long-term tests. In the LT-grown film, although the films became Sr-terminated after long-term annealing, surface restructuring enabled catalytically active cobalt to reach stoichiometry immediately below the outermost-surface layer. This study shows that thermally induced chemical restructuring is particularly important for the stability of LSC64 electrodes.

■ ASSOCIATED CONTENT

Supporting Information

The Supporting Information is available free of charge at https://pubs.acs.org/doi/10.1021/acsami.0c08308.

SEM, XPS, LEIS, IEDP−SIMS fittings, EIS data, and additional table (PDF)

■ AUTHOR INFORMATION

Corresponding Author

Ozden Celikbilek − *Department of Materials, Imperial College London, London SW7 2BP, United Kingdom;* orcid.org/0000-0001-6287-9119; Email: o.celikbilek@imperial.ac.uk

Authors

Andrea Cavallaro − *Department of Materials, Imperial College London, London SW7 2BP, United Kingdom*

Gwilherm Kerherve − *Department of Materials, Imperial College London, London SW7 2BP, United Kingdom*

Sarah Fearn − *Department of Materials, Imperial College London, London SW7 2BP, United Kingdom*

Odette Chaix-Pluchery − *Université Grenoble Alpes, CNRS, Grenoble INP, LMGP, Grenoble 38000, France*

Ainara Aguadero − *Department of Materials, Imperial College London, London SW7 2BP, United Kingdom;* orcid.org/0000-0001-7098-1033

John A. Kilner − *Department of Materials, Imperial College London, London SW7 2BP, United Kingdom; International Institute for Carbon-Neutral Energy Research (I2CNER), Kyushu University, Fukuoka 819-0395, Japan*

Stephen J. Skinner − *Department of Materials, Imperial College London, London SW7 2BP, United Kingdom;* orcid.org/0000-0001-5446-2647

Complete contact information is available at: https://pubs.acs.org/10.1021/acsami.0c08308

Author Contributions

O.C. carried out laboratory research and wrote the draft of the manuscript. A.C. carried out oxygen transport kinetics experiments, advised on the methodology. G.K. conducted XPS measurements and data analyses. S.F. performed the SIMS analyses. O.C.-P. analysed and interpreted the Raman spectroscopy experiments. A.A. and J.A.K. advised on the critical revision of the manuscript; S.J.S. supervised the project. The manuscript was revised through the contributions of all authors. All authors have approved the final version of the manuscript.

Notes

The authors declare no competing financial interest.

https://dx.doi.org/10.1021/acsami.0c08308
ACS Appl. Mater. Interfaces 2020, 12, 34388−34401

■ ACKNOWLEDGMENTS

The authors thank Richard Sweeney and Dr. Victoria Bemmer for their assistance in XRD and AFM operations, Dr. Federico Pesci for the operational enquiries for Raman spectroscopy, and Nicolas J. Williams with the drawing of the sketch in Figure 10. This project has received funding from the European Union's Horizon 2020 research and innovation programme under the Marie Sklodowska-Curie grant agreement no. 836503, and under grant agreement No 824072 (Harvestore). J.A.K. acknowledges the support of Solid Oxide Interfaces for Faster Ion Transport (SOIFIT) JSPS/EPSRC (EP/P026478/1) Core-to-Core Program (Advanced Research Networks). The authors also acknowledge funding from the EPSRC grant (EP/M014142/1).

■ REFERENCES

(1) Acosta, M.; Baiutti, F.; Tarancón, A.; MacManus-Driscoll, J. L. Nanostructured Materials and Interfaces for Advanced Ionic Electronic Conducting Oxides. *Adv. Mater. Interfaces* **2019**, *6*, 1900462.

(2) Garbayo, I.; Baiutti, F.; Morata, A.; Tarancón, A. Engineering Mass Transport Properties in Oxide Ionic and Mixed Ionic-Electronic Thin Film Ceramic Conductors for Energy Applications. *J. Eur. Ceram. Soc.* **2019**, *39*, 101−114.

(3) Skinner, S. J. Recent Advances in the Understanding of the Evolution of Surfaces and Interfaces in Solid Oxide Cells. *Adv. Mater. Interfaces* **2019**, *6*, 1900580.

(4) Koo, B.; Kim, K.; Kim, J. K.; Kwon, H.; Han, J. W.; Jung, W. Sr Segregation in Perovskite Oxides: Why It Happens and How It Exists. *Joule* **2018**, *2*, 1476−1499.

(5) dos Santos-Gómez, L.; Porras-Vázquez, J. M.; Losilla, E. R.; Martín, F.; Ramos-Barrado, J. R.; Marrero-López, D. Stability and performance of La0.6Sr0.4Co0.2Fe0.8O3-δ nanostructured cathodes with Ce0.8Gd0.2O1.9 surface coating. *J. Power Sources* **2017**, *347*, 178−185.

(6) Ovenstone, J.; White, J. S.; Misture, S. T. Phase transitions and phase decomposition of La1−xSrxCoO3−δ in low oxygen partial pressures. *J. Power Sources* **2008**, *181*, 56−61.

(7) Celikbilek, O.; Thieu, C.-A.; Agnese, F.; Calì, E.; Lenser, C.; Menzler, N. H.; Son, J.-W.; Skinner, S. J.; Djurado, E. Enhanced catalytic activity of nanostructured, A-site deficient (La0.7Sr0.3)0.95-(Co0.2Fe0.8)O3−δ for SOFC cathodes. *J. Mater. Chem. A* **2019**, *7*, 25102−25111.

(8) Infortuna, A.; Harvey, A. S.; Gauckler, L. J. Microstructures of CGO and YSZ Thin Films by Pulsed Laser Deposition. *Adv. Funct. Mater.* **2008**, *18*, 127−135.

(9) Heiroth, S.; Frison, R.; Rupp, J. L. M.; Lippert, T.; Barthazy Meier, E. J.; Müller Gubler, E.; Döbeli, M.; Conder, K.; Wokaun, A.; Gauckler, L. J. Crystallization and Grain Growth Characteristics of Yttria-Stabilized Zirconia Thin Films Grown by Pulsed Laser Deposition. *Solid State Ionics* **2011**, *191*, 12−23.

(10) Tripković, D.; Küngas, R.; Mogensen, M. B.; Hendriksen, P. V. Surface Recrystallization-an Underestimated Phenomenon Affecting Oxygen Exchange Activity. *J. Mater. Chem. A* **2019**, *7*, 11782−11791.

(11) Efimov, V.; Efimova, E.; Karpinsky, D.; Kochubey, D. I.; Kriventsov, V.; Kuzmin, A.; Molodtsov, S.; Sikolenko, V.; Tiutiunnikov, S.; Troyanchuk, I. O.; Shmakov, A. N.; Vyalikh, D. XAFS and neutron diffraction study of the La1-xSrxCoO3. *Phys. Status Solidi C* **2007**, *4*, 805−808.

(12) Sitte, W.; Bucher, E.; Preis, W. Nonstoichiometry and Transport Properties of Strontium-Substituted Lanthanum Cobaltites. *Solid State Ionics* **2002**, *154−155*, 517−522.

(13) Yu, Y.; Ludwig, K. F.; Woicik, J. C.; Gopalan, S.; Pal, U. B.; Kaspar, T. C.; Basu, S. N. Effect of Sr Content and Strain on Sr Surface Segregation of La1-xSrxCo0.2Fe0.8O3−δ as Cathode Material for Solid Oxide Fuel Cells. *ACS Appl. Mater. Interfaces* **2016**, *8*, 26704−26711.

(14) Lu, Y.; Kreller, C.; Adler, S. B. Measurement and Modeling of the Impedance Characteristics of Porous La1-xSrxCoO3−δ Electrodes. *J. Electrochem. Soc.* **2009**, *156*, B513−B525.

(15) Zhu, Z.; Shi, Y.; Aruta, C.; Yang, N. Improving Electronic Conductivity and Oxygen Reduction Activity in Sr-Doped Lanthanum Cobaltite Thin Films: Cobalt Valence State and Electronic Band Structure Effects. *ACS Appl. Energy Mater.* **2018**, *1*, 5308−5317.

(16) Januschewsky, J.; Ahrens, M.; Opitz, A.; Kubel, F.; Fleig, J. Optimized La0.6Sr0.4CoO3-δThin-Film Electrodes with Extremely Fast Oxygen-Reduction Kinetics. *Adv. Funct. Mater.* **2009**, *19*, 3151−3156.

(17) Evans, A.; Martynczuk, J.; Stender, D.; Schneider, C. W.; Lippert, T.; Prestat, M. Low-Temperature Micro-Solid Oxide Fuel Cells with Partially Amorphous La0.6Sr0.4CoO3-δ Cathodes. *Adv. Energy Mater.* **2015**, *5*, 1400747.

(18) Kubicek, M.; Limbeck, A.; Frömling, T.; Hutter, H.; Fleig, J. Relationship between Cation Segregation and the Electrochemical Oxygen Reduction Kinetics of La0.6Sr0.4CoO3−δ Thin Film Electrodes. *J. Electrochem. Soc.* **2011**, *158*, B727−B734.

(19) Cai, Z.; Kubicek, M.; Fleig, J.; Yildiz, B. Chemical Heterogeneities on La0.6Sr0.4CoO3−δ Thin Films-Correlations to Cathode Surface Activity and Stability. *Chem. Mater.* **2012**, *24*, 1116−1127.

(20) Kubicek, M.; Rupp, G. M.; Huber, S.; Penn, A.; Opitz, A. K.; Bernardi, J.; Stöger-Pollach, M.; Hutter, H.; Fleig, J. Cation diffusion in La0.6Sr0.4CoO3−δ below 800 °C and its relevance for Sr segregation. *Phys. Chem. Chem. Phys.* **2014**, *16*, 2715−2726.

(21) Rupp, G. M.; Téllez, H.; Druce, J.; Limbeck, A.; Ishihara, T.; Kilner, J.; Fleig, J. Surface chemistry of La0.6Sr0.4CoO3−δ thin films and its impact on the oxygen surface exchange resistance. *J. Mater. Chem. A* **2015**, *3*, 22759−22769.

(22) Chen, T.; Harrington, G. F.; Masood, J.; Sasaki, K.; Perry, N. H. Emergence of Rapid Oxygen Surface Exchange Kinetics during in Situ Crystallization of Mixed Conducting Thin Film Oxides. *ACS Appl. Mater. Interfaces* **2019**, *11*, 9102−9116.

(23) Chen, T.; Harrington, G. F.; Sasaki, K.; Perry, N. H. Impact of Microstructure and Crystallinity on Surface Exchange Kinetics of Strontium Titanium Iron Oxide Perovskite by in Situ Optical Transmission Relaxation Approach. *J. Mater. Chem. A* **2017**, *5*, 23006−23019.

(24) Cavallaro, A.; Pramana, S. S.; Ruiz-Trejo, E.; Sherrell, P. C.; Ware, E.; Kilner, J. A.; Skinner, S. J. Amorphous-Cathode-Route towards Low Temperature SOFC. *Sustainable Energy Fuels* **2018**, *2*, 862−875.

(25) Nečas, D.; Klapetek, P. Gwyddion: An Open-Source Software for SPM Data Analysis. *Cent. Eur. J. Phys.* **2012**, *10*, 181−188.

(26) Thermo Fisher Scientific. *Avantage Software*. https://xpssimplified.com/avantage_data_system.ph, 2019.

(27) Killoran, D. R. The Effective Duration of a Linear Slow-Cool. *J. Electrochem. Soc.* **1962**, *109*, 170−171.

(28) Cooper, S. J.; Niania, M.; Hoffmann, F.; Kilner, J. A. Back-Exchange: A Novel Approach to Quantifying Oxygen Diffusion and Surface Exchange in Ambient Atmospheres. *Phys. Chem. Chem. Phys.* **2017**, *19*, 12199−12205.

(29) Garbayo, I.; Tarancón, A.; Santiso, J.; Peiró, F.; Alarcón-LLadó, E.; Cavallaro, A.; Gràcia, I.; Cané, C.; Sabaté, N. Electrical Characterization of Thermomechanically Stable YSZ Membranes for Micro Solid Oxide Fuel Cells Applications. *Solid State Ionics* **2010**, *181*, 322−331.

(30) Ullmann, H.; Trofimenko, N.; Tietz, F.; Stöver, D.; Ahmad-Khanlou, A.; Stöver, D.; Ahmad-Khanlou, A. Correlation between Thermal Expansion and Oxide Ion Transport in Mixed Conducting Perovskite-Type Oxides for SOFC Cathodes. *Solid State Ionics* **2000**, *138*, 79−90.

(31) Heel, A.; Holtappels, P.; Hug, P.; Graule, T. Flame Spray Synthesis of Nanoscale La0.6Sr0.4Co0.2Fe0.8O3-δ and Ba0.5Sr0.5-Co0.8Fe0.2O3-δ as Cathode Materials for Intermediate Temperature Solid Oxide Fuel Cells. *Fuel Cells* **2010**, *10*, 419−432.

https://dx.doi.org/10.1021/acsami.0c08308
ACS Appl. Mater. Interfaces 2020, 12, 34388−34401

(32) Plonczak, P.; Bieberle-Hütter, A.; Søgaard, M.; Ryll, T.; Martynczuk, J.; Hendriksen, P. V.; Gauckler, L. J. Tailoring of LaxSr1−xCoyFe1−yO3−δ Nanostructure by Pulsed Laser Deposition. *Adv. Funct. Mater.* **2011**, *21*, 2764−2775.
(33) Rupp, J. L. M.; Scherrer, B.; Gauckler, L. J. Engineering Disorder in Precipitation-Based Nano-Scaled Metal Oxide Thin Films. *Phys. Chem. Chem. Phys.* **2010**, *12*, 11114.
(34) Iliev, M. N.; Abrashev, M. V.; Popov, V. N.; Hadjiev, V. G. Role of Jahn-Teller Disorder in Raman Scattering of Mixed-Valence Manganites. *Phys. Rev. B: Condens. Matter Mater. Phys.* **2003**, *67*, 212301.
(35) Orlovskaya, N.; Steinmetz, D.; Yarmolenko, S.; Pai, D.; Sankar, J.; Goodenough, J. Detection of Temperature- and Stress-Induced Modifications of LaCoO3 by Micro-Raman Spectroscopy. *Phys. Rev. B: Condens. Matter Mater. Phys.* **2005**, *72*, 014122.
(36) Maris, G.; Ren, Y.; Volotchaev, V.; Zobel, C.; Lorenz, T.; Palstra, T. T. M. Evidence for Orbital Ordering in LaCoO3. *Phys. Rev. B: Condens. Matter Mater. Phys.* **2003**, *67*, 224423.
(37) Takami, T.; Zhou, J. S.; Goodenough, J. B.; Ikuta, H. Correlation between the Structure and the Spin State in R1-XSrxCoO3 (R=La, Pr, and Nd). *Phys. Rev. B: Condens. Matter Mater. Phys.* **2007**, *76*, 144116.
(38) Ishikawa, A.; Nohara, J.; Sugai, S. Raman Study of the Orbital-Phonon Coupling in LaCoO3. *Phys. Rev. Lett.* **2004**, *93*, 136401.
(39) Li, X.; Peng, Z.; Fan, W.; Guo, K.; Gu, J.; Zhao, M.; Meng, J. Raman Spectra Study of Nanocrystalline Composite Oxides. *Mater. Chem. Phys.* **1996**, *46*, 50−54.
(40) Bak, T.; Nowotny, J.; Rekas, M.; Ringer, S.; Sorrell, C. C. Defect chemistry and electrical properties of La1−xSrxCoO3−δ III. Oxygen nonstoichiometry. *Ionics* **2001**, *7*, 380−387.
(41) Tsvetkov, N.; Lu, Q.; Sun, L.; Crumlin, E. J.; Yildiz, B. Improved Chemical and Electrochemical Stability of Perovskite Oxides with Less Reducible Cations at the Surface. *Nat. Mater.* **2016**, *15*, 1010−1016.
(42) Wen, Y.; Yang, T.; Lee, D.; Lee, H. N.; Crumlin, E. J.; Huang, K. Temporal and thermal evolutions of surface Sr-segregation in pristine and atomic layer deposition modified La0.6Sr0.4CoO3−δ epitaxial films. *J. Mater. Chem. A* **2018**, *6*, 24378−24388.
(43) Cheng, X.; Fabbri, E.; Nachtegaal, M.; Castelli, I. E.; El Kazzi, M.; Haumont, R.; Marzari, N.; Schmidt, T. J. Oxygen Evolution Reaction on La1-xSrxCoO3 Perovskites: A Combined Experimental and Theoretical Study of Their Structural, Electronic, and Electrochemical Properties. *Chem. Mater.* **2015**, *27*, 7662−7672.
(44) Jalili, H.; Han, J. W.; Kuru, Y.; Cai, Z.; Yildiz, B. New Insights into the Strain Coupling to Surface Chemistry, Electronic Structure, and Reactivity of La0.7Sr0.3MnO3. *J. Phys. Chem. Lett.* **2011**, *2*, 801−807.
(45) Niania, M.; Podor, R.; Britton, T. B.; Li, C.; Cooper, S. J.; Svetkov, N.; Skinner, S.; Kilner, J. In situ study of strontium segregation in La0.6Sr0.4Co0.2Fe0.8O3−δ in ambient atmospheres using high-temperature environmental scanning electron microscopy. *J. Mater. Chem. A* **2018**, *6*, 14120−14135.
(46) Egger, A.; Perz, M.; Bucher, E.; Gspan, C.; Sitte, W. Effect of Microstructure on the Degradation of La0.6Sr0.4CoO3−δ Electrodes in Dry and Humid Atmospheres. *Fuel Cells* **2019**, *19*, 458−471.
(47) Kim, J.-G.; Pugmire, D. L.; Battaglia, D.; Langell, M. A. Analysis of the NiCo2O4 Spinel Surface with Auger and X-Ray Photoelectron Spectroscopy. *Appl. Surf. Sci.* **2000**, *165*, 70−84.
(48) Vaz, C. A. F.; Prabhakaran, D.; Altman, E. I.; Henrich, V. E. Experimental Study of the Interfacial Cobalt Oxide in Co3O4/α-Al2O3 (0001) Epitaxial Films. *Phys. Rev. B: Condens. Matter Mater. Phys.* **2009**, *80*, 155457.
(49) Mizokawa, T.; Tjeng, L. H.; Steeneken, P. G.; Brookes, N. B.; Tsukada, I.; Yamamoto, T.; Uchinokura, K. Photoemission and X-Ray-Absorption Study of Misfit-Layered (Bi,Pb)-Sr-Co-O Compounds: Electronic Structure of a Hole-Doped Co-O Triangular Lattice. *Phys. Rev. B: Condens. Matter Mater. Phys.* **2001**, *64*, 115104.
(50) Nenning, A.; Opitz, A. K.; Rameshan, C.; Rameshan, R.; Blume, R.; Hävecker, M.; Knop-Gericke, A.; Rupprechter, G.; Klötzer, B.; Fleig, J. Ambient Pressure XPS Study of Mixed Conducting Perovskite-Type SOFC Cathode and Anode Materials under Well-Defined Electrochemical Polarization. *J. Phys. Chem. C* **2016**, *120*, 1461−1471.
(51) Druce, J.; Téllez, H.; Burriel, M.; Sharp, M. D.; Fawcett, L. J.; Cook, S. N.; McPhail, D. S.; Ishihara, T.; Brongersma, H. H.; Kilner, J. A. Surface Termination and Subsurface Restructuring of Perovskite-Based Solid Oxide Electrode Materials. *Energy Environ. Sci.* **2014**, *7*, 3593−3599.
(52) Zameshin, A. A.; Yakshin, A. E.; Sturm, J. M.; Brongerma, H. H.; Bijkerk, F. Double Matrix Effect in Low Energy Ion Scattering from La Surfaces. *Appl. Surf. Sci.* **2018**, *440*, 570−579.
(53) Berenov, A. V.; Atkinson, A.; Kilner, J. A.; Bucher, E.; Sitte, W. Oxygen tracer diffusion and surface exchange kinetics in La0.6Sr0.4-CoO3−δ. *Solid State Ionics* **2010**, *181*, 819−826.
(54) Wang, Z.; Liu, B.; Zhao, E. W.; Jin, K.; Du, Y.; Neeway, J. J.; Ryan, J. V.; Hu, D.; Zhang, K. H. L.; Hong, M.; Le Guernic, S.; Thevuthasan, S.; Wang, F.; Zhu, Z. Argon Cluster Sputtering Source for ToF-SIMS Depth Profiling of Insulating Materials: High Sputter Rate and Accurate Interfacial Information. *J. Am. Soc. Mass Spectrom.* **2015**, *26*, 1283−1290.
(55) Druce, J.; Ishihara, T.; Kilner, J. Surface Composition of Perovskite-Type Materials Studied by Low Energy Ion Scattering (LEIS). *Solid State Ionics* **2014**, *262*, 893−896.
(56) Opitz, A. K.; Rameshan, C.; Kubicek, M.; Rupp, G. M.; Nenning, A.; Götsch, T.; Blume, R.; Hävecker, M.; Knop-Gericke, A.; Rupprechter, G.; Klötzer, B.; Fleig, J. The Chemical Evolution of the La0.6Sr0.4CoO3−δ Surface Under SOFC Operating Conditions and Its Implications for Electrochemical Oxygen Exchange Activity. *Top. Catal.* **2018**, *61*, 2129−2141.
(57) Kotomin, E. A.; Mastrikov, Y. A.; Merkle, R.; Maier, J. First Principles Calculations of Oxygen Reduction Reaction at Fuel Cell Cathodes. *Curr. Opin. Electrochem.* **2020**, *19*, 122−128.
(58) Cao, Y.; Gadre, M. J.; Ngo, A. T.; Adler, S. B.; Morgan, D. D. Factors Controlling Surface Oxygen Exchange in Oxides. *Nat. Commun.* **2019**, *10*, 1346.
(59) Rupp, G. M.; Opitz, A. K.; Nenning, A.; Limbeck, A.; Fleig, J. Real-Time Impedance Monitoring of Oxygen Reduction during Surface Modification of Thin Film Cathodes. *Nat. Mater.* **2017**, *16*, 640−645.
(60) Mogensen, M. B.; Chatzichristodoulou, C.; Graves, C.; Hansen, K. V.; Hansen, K. K.; Hauch, A.; Jacobsen, T.; Norrman, K. New Hypothesis for SOFC Ceramic Oxygen Electrode Mechanisms. *ECS Trans.* **2016**, *72*, 93−103.
(61) Staykov, A.; Téllez, H.; Akbay, T.; Druce, J.; Ishihara, T.; Kilner, J. Oxygen Activation and Dissociation on Transition Metal Free Perovskite Surfaces. *Chem. Mater.* **2015**, *27*, 8273−8281.
(62) Staykov, A.; Tellez, H.; Druce, J.; Wu, J.; Ishihara, T.; Kilner, J. Electronic Properties and Surface Reactivity of SrO-Terminated SrTiO3 and SrO-Terminated Iron-Doped SrTiO3. *Sci. Technol. Adv. Mater.* **2018**, *19*, 221−230.
(63) Téllez, H.; Druce, J.; Ishihara, T.; Kilner, J. A. (Invited) Effects of Microstructure on Surface Segregation: Role of Grain Boundaries. *ECS Trans.* **2016**, *72*, 57−69.
(64) Pişkin, F.; Bliem, R.; Yildiz, B. Effect of Crystal Orientation on the Segregation of Aliovalent Dopants at the Surface of La0.6Sr0.4CoO3. *J. Mater. Chem. A* **2018**, *6*, 14136−14145.
(65) Fearn, S.; Rossiny, J. C. H.; Kilner, J. A.; Evans, J. R. G. Measurement of oxygen transport in La0.8Sr0.2MnO3 perovskite grains. *Solid State Ionics* **2012**, *211*, 51−57.
(66) Burriel, M.; Peña-Martínez, J.; Chater, R. J.; Fearn, S.; Berenov, A. V.; Skinner, S. J.; Kilner, J. A. Anisotropic Oxygen Ion Diffusion in Layered PrBaCo2O5+δ. *Chem. Mater.* **2012**, *24*, 613−621.
(67) Burriel, M.; Garcia, G.; Santiso, J.; Kilner, J. A.; Chater, R. J.; Skinner, S. J. Anisotropic oxygen diffusion properties in epitaxial thin films of La2NiO4+δ. *J. Mater. Chem.* **2008**, *18*, 416−422.
(68) Chen, Y.; Téllez, H.; Burriel, M.; Yang, F.; Tsvetkov, N.; Cai, Z.; McComb, D. W.; Kilner, J. A.; Yildiz, B. Segregated Chemistry and Structure on (001) and (100) Surfaces of (La1-xSrx)2CoO4 Override

https://dx.doi.org/10.1021/acsami.0c08308
ACS Appl. Mater. Interfaces 2020, 12, 34388−34401

the Crystal Anisotropy in Oxygen Exchange Kinetics. *Chem. Mater.* **2015**, *27*, 5436−5450.
(69) Burriel, M.; Téllez, H.; Chater, R. J.; Castaing, R.; Veber, P.; Zaghrioui, M.; Ishihara, T.; Kilner, J. A.; Bassat, J.-M. Influence of Crystal Orientation and Annealing on the Oxygen Diffusion and Surface Exchange of La2NiO4+δ. *J. Phys. Chem. C* **2016**, *120*, 17927−17938.
(70) Develos-Bagarinao, K.; De Vero, J.; Kishimoto, H.; Ishiyama, T.; Yamaji, K.; Horita, T.; Yokokawa, H. Oxygen surface exchange properties and surface segregation behavior of nanostructured La0.6Sr0.4Co0.2Fe0.8O3−δ thin film cathodes. *Phys. Chem. Chem. Phys.* **2019**, *21*, 7183−7195.

https://dx.doi.org/10.1021/acsami.0c08308
ACS Appl. Mater. Interfaces 2020, 12, 34388−34401